RESEARCH   **Open Access**

Imaging of polymer:fullerene bulk-heterojunctions in a scanning electron microscope: methodology aspects and nanomorphology by correlative SEM and STEM

Yonghe Li[1,3,4]* , Erich Müller[1,3], Christian Sprau[2,3], Alexander Colsmann[2,3] and Dagmar Gerthsen[1,3,4]

Abstract

Scanning transmission electron microscopy (STEM) at low energies (≤ 30 keV) in a scanning electron microscope is well suited to distinguish weakly scattering materials with similar materials properties and analyze their microstructure. The capabilities of the technique are illustrated in this work to resolve material domains in $PTB7:PC_{71}BM$ bulk-heterojunctions, which are commonly implemented for light-harvesting in organic solar cells. Bright-field (BF-) and high-angle annular dark-field (HAADF-) STEM contrast of pure PTB7 and $PC_{71}BM$ was first systematically analyzed using a wedge-shaped sample with well-known thickness profile. Monte-Carlo simulations are essential for the assignment of material contrast for materials with only slightly different scattering properties. Different scattering cross-sections were tested in Monte-Carlo simulations with screened Rutherford scattering cross-sections yielding best agreement with the experimental data. The STEM intensity also depends on the local specimen thickness, which can be dealt with by correlative STEM and scanning electron microscopy (SEM) imaging of the same specimen region yielding additional topography information. Correlative STEM/SEM was applied to determine the size of donor (PTB7) and acceptor ($PC_{71}BM$) domains in $PTB7:PC_{71}BM$ absorber layers that were deposited from solution with different contents of the processing additive 1,8-diiodooctane (DIO).

Keywords: Low-energy scanning transmission electron microscopy, TSEM, STEM-in-SEM, Scanning electron microscopy, PTB7, $PC_{71}BM$, Organic solar cells, Nanomorphology

Introduction

Lowering the electron energy from 80 keV and above in standard scanning transmission electron microscopy (STEM) experiments to 30 keV in scanning electron microscopes equipped with a STEM detector leads to the suppression of knock-on damage and contrast enhancement due to the increased scattering probability [1–3].

The latter is favorable to distinguish weakly scattering materials with similar material densities and average atomic numbers. Although STEM resolution in scanning electron microscopes is still lower than in transmission electron microscopes, best instruments meanwhile provide a spatial resolution of ∼ 0.34 nm which is sufficient to tackle numerous materials problems [4, 5]. Another advantage of scanning electron microscopes is the inherent availability of surface topography imaging by secondary-electron scanning electron microscopy (SE-SEM), which can be correlatively applied in combination with STEM. This means that SEM and STEM images are

*Correspondence: yonghe.li2@kit.edu
[1] Laboratory for Electron Microscopy, Karlsruhe Institute of Technology (KIT), Engesserstr. 7, 76131 Karlsruhe, Germany
Full list of author information is available at the end of the article

Li *et al. Adv Struct Chem Imag*   (2020) 6:2

Page 2 of 12

acquired in parallel revealing surface topography and bulk structure from exactly the same specimen region [6–8]. This capability is important because STEM contrast can be influenced by topography effects and SE-SEM images support the interpretation of STEM images.

Despite of these advantages, low-energy STEM (≤ 30 keV) in a scanning electron microscope (also denoted as STEM-in-SEM) has not been extensively exploited up to now and only few methodological studies were published [9–11]. More recent work comprises, e.g., nanoparticle characterization [12, 13], dislocations analysis and manipulation [14–17], composition quantification [18], beam broadening [19, 20], transmission electron microscopy (TEM) specimen thickness determination [21] as well as reduced delocalization and negligible Cherenkov losses in electron energy loss spectroscopy [22]. Low-energy STEM is also well suited to study weakly scattering and beam-sensitive (knock-on damage) materials such as bulk-heterojunction (BHJ) absorber layers of organic solar cells [23]. BHJ absorber layers consist of an interpenetrating network of domains of donor and acceptor molecules with domain sizes, which are, typically, in the order of a few 10 nm for best power conversion efficiencies. The morphology of these layers, especially the domain size, phase distribution and degree of phase separation must be optimized during device fabrication and influences every aspect of the photovoltaic energy conversion process, such as charge carrier separation and charge carrier mobility [24]. Studying phase separation in BHJs on the nanoscale allows the correlation of the nanomorphology and the power conversion efficiency.

Up to now, standard (S)TEM imaging at energies ≥ 80 keV is typically applied to characterize phase separation in absorber layers [25, 26] but may lead to knock-on damage and low material contrast [27, 28]. The contrast can be enhanced in TEM imaging by defocusing, but this leads to a significant loss of resolution [29]. It was also shown that TEM imaging of the domain morphology may not be sufficient to distinguish thickness variations and material contrast. Additional topography information is often needed by applying atomic force microscopy (AFM) imaging [30]. Although previous work [23, 31] has profited from low-energy STEM to study the size and distribution of donor and acceptor domains in polyhexylthiophene:fullerene and polyselenophene:fullerene absorber layers, STEM contrast interpretation still required additional AFM experiments to assess possible thickness changes in the TEM samples. Due to the small scale of the domain structures and change of instrumentation, AFM and TEM images often cannot be obtained from the same sample region. In contrast, correlative low-energy STEM/SE-SEM is

distinctly more advantageous as it yields volume and topography information from exactly the same specimen region.

Previous work has already demonstrated that simulations of the STEM intensity are helpful or even indispensable for the assignment of material contrast. This applies in particular if blends of materials with similar material properties (material density, average atomic number, average atomic weight) are investigated [23]. Monte-Carlo (MC) simulations are commonly used for simulations of the STEM intensity, but different types of scattering cross-sections (screened Rutherford and Mott cross-sections) exist. However, the choice of the most adequate scattering cross-section is not always obvious and can lead to significantly varying results [21].

In this work, we propose to apply correlative low-energy STEM/SE-SEM to characterize the nanomorphology of BHJ absorber layers containing the donor poly [(4,8-bis [(2-ethylhexyl) oxy] benzo [1,2-b:4,5-b'] dithiophene-2,6-diyl] [3-fluoro-2-[(2-ethylhexyl) carbonyl] thieno [3,4-b] thiophenediyl]] (PTB7, $C_{41}H_{53}FO_4S_4$) and the acceptor [6]-phenyl C_{71}-butric acid methyl ester (PC$_{71}$BM, $C_{82}H_{14}O_2$) [32]. When deposited from *o*-xylene solution, the power conversion efficiency (PCE) of PTB7:PC$_{71}$BM absorber layers is substantially improved upon addition of the co-solvent 1,8-diiodooctane (DIO) with volume contents up to 3% [33] which is commonly attributed to a change of the nanomorphology of the absorber layers. Due to the similarity of scattering properties of PTB7 and PC$_{71}$BM, we first performed a systematic study of the contrast of pure PC$_{71}$BM and PTB7 by bright-field (BF-) STEM and high-angle annular dark-field (HAADF-) STEM as a function of sample thickness and primary electron energy. To determine the suitable scattering cross-section, we have compared experimental and simulated STEM intensities of the pure materials using a model sample with wedge-type geometry with known thickness profile. Based on the established methodology, correlative SEM and STEM imaging of PTB7:PC$_{71}$BM blends then yields detailed insights into the nanomorphology of the layers, i.e. domain size, domain distribution and surface topography, as well as the influence of DIO on the bulk-heterojunction formation.

Materials and methods
Layer preparation and sample preparation for electron microscopy
The photoactive layers were prepared on indium tin oxide (ITO) coated glass substrates by solution-deposition of a sacrificial layer of poly(3,4-ethylenedioxythiophene):polystyrene sulfonate (PEDOT:PSS, Clevios VPAI 4083, Heraeus). PTB7 ($C_{41}H_{53}FO_4S_4$, 1-Material Inc.) and

Li *et al. Adv Struct Chem Imag*   (2020) 6:2

Page 3 of 12

$PC_{71}BM$ ($C_{82}H_{14}O_2$, Solenne BV) were dissolved (1:1.5 w/w, total concentration 25 mg mL^{-1}) in *o*-xylene (Sigma-Aldrich, anhydrous, 97%) at 85 °C overnight. Then, 1 vol% or 3 vol% of the solvent additive 1,8-diiodooctane (DIO, Alfa Aesar, 98%) was added. The $PTB7:PC_{71}BM$ layer was spin cast (1500 rpm, 60 s, 90 nm) from the warm solution (85 °C) atop PEDOT:PSS and dried at room temperature. More details on absorber layer fabrication are described in the literature [33]. For contrast analysis of the pure materials, PTB7 and $PC_{71}BM$ layers were deposited on PEDOT:PSS coated ITO substrates.

Plan-view samples of $PTB7:PC_{71}BM$ bulk-heterojunction absorber layers for correlative STEM/SEM were prepared by the following procedure. $PTB7:PC_{71}BM$ absorber layers deposited on PEDOT:PSS-coated ITO substrates were cut into small pieces with a scalpel. As PEDOT:PSS is water soluble, the layer pieces were floated off the substrate by a drop of water and picked up by a TEM grid. The same procedure was used for the pure PTB7 and $PC_{71}BM$ layers. A model sample for STEM contrast analyses was prepared by alternately stacking the detached PTB7 and $PB_{71}BM$ layers on a Si substrate. Two cross-sections specimens of the $PTB7/PC_{71}BM$ layer stack were prepared by focused-ion-beam (FIB) milling. One sample was prepared with a wedge shape (wedge angle 20 degrees) to obtain a specimen with a priori known thicknesses. Another cross-section specimen was prepared with a constant thickness. Electron- and ion-beam-induced Pt deposition was first employed to protect the layer system during FIB milling. A thick lamella was first prepared with 30 keV Ga ions and a large Ga-ion current. Further thinning was carried out with a reduced ion current of 41 pA. A low ion current of 12 pA and 5 keV Ga ions were used for final polishing to minimize damage and achieve smooth sample surfaces.

Experimental setup

Sample preparation by FIB milling and STEM/SEM imaging was in both cases performed in a Helios G4 FX dual-beam microscope (Thermo Fisher Scientific, USA) equipped with a field emission electron gun and Ga-ion column. Topography imaging was performed by collecting secondary electrons with the Everhart-Thornley Detector (ETD). A retractable e-Flash^{HR} charge-coupled-device (CCD) camera implemented in a Bruker OPTI-MUS^{TM} camera head is mounted below the specimen for acquiring on-axis transmission electron diffraction (TED) patterns. Furthermore, a multi-segmented STEM detector is positioned 40 mm below the objective lens pole piece. The STEM detector contains a small inner segment for BF imaging followed by four annular dark-field (ADF) rings and a HAADF detector segment. The detection-angle range of the different segments is determined by

the inner and outer radii of the detector segments and the distance between the sample and STEM detector. The latter is 36 mm and the working distance (WD) between specimen and objective lens pole piece was chosen to be 4 mm in this work. Accordingly, electrons are collected up to 6.9 mrad by the BF segment. The collection-angle range of the HAADF–STEM segment covers 67.8 to 271 mrad. Primary electron energies from 10 to 30 keV were used for imaging of energy-related effects. A special accessory of the Helios G4 FX is a double-tilt specimen holder for the investigation of electron-transparent specimens.

In this work, we quantitatively compare experimental and simulated STEM intensities. For this purpose, measured STEM intensities must be normalized with respect to the intensity of the incident electron beam. For the acquisition of the experimental STEM intensity we use the following procedure. First, the detector is directly illuminated without sample to measure the intensity of the incident electron beam. Contrast and brightness are adjusted that the BF or HAADF detector appears white with a gray level intensity (I_w) close to 65,535 for our 16-bit STEM detector. Inactive ADF detector segments appear black with a gray level intensity (I_b) close to zero. Over- and undersaturation has to be strictly avoided during the procedure. Contrast and brightness settings must remain unchanged for subsequent specimen imaging. For illustration, Fig. 1a shows a STEM image of the illuminated BF segment with the adjacent black ADF segment after optimization of contrast and brightness. The normalized BF–STEM intensity $I_{Norm.BF}$ of a sample with measured intensity I_s is then given by Eq. (1).

$$I_{Norm.BF} = \frac{I_s - I_b}{I_w - I_b} \tag{1}$$

Figure 1b shows a STEM image of the innermost part of the illuminated HAADF and the adjacent black ADF region. The normalized HAADF–STEM intensity $I_{Norm.HAADF}$ is given by Eq. (2).

$$I_{Norm.HAADF} = \frac{I_s - I_b}{(1 - \varepsilon)I_w - I_b} \tag{2}$$

Here, the factor ε takes into account that an in transparent aperture with six supporting bars is positioned above the detector ($\varepsilon_1 = 8.25\%$). The HAADF intensity is further reduced by impurities (e.g. particles) and dark lines on the HAADF detector ($\varepsilon_2 = \sim 7.6\%$) (cf. Fig. 1b).

To improve the visibility of STEM images with low contrast, images were in some cases post-processed in the following way. According to the intensity histogram, gray levels were rescaled for the minimum and maximum
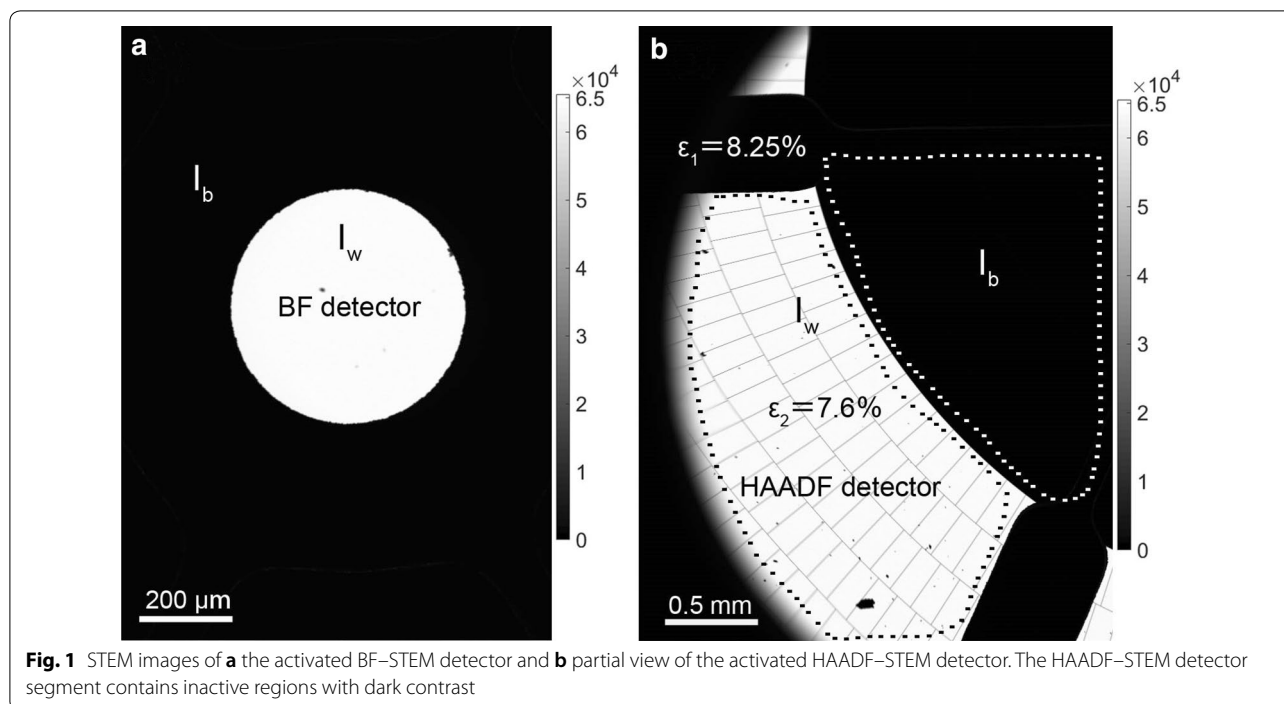
Li *et al. Adv Struct Chem Imag* (2020) 6:2

Page 4 of 12

Fig. 1 STEM images of **a** the activated BF–STEM detector and **b** partial view of the activated HAADF–STEM detector. The HAADF–STEM detector segment contains inactive regions with dark contrast

intensities to cover the full grayscale range between 0 and 255.

Energy-filtered transmission electron microscopy (EFTEM) was performed to measure thickness profiles of the prepared wedge-shaped specimens. EFTEM was performed with a Titan3 80–300 transmission electron microscope (formerly FEI now Thermo Fisher Scientific, USA) operated at 300 keV and equipped with a Gatan Tridiem 655 HR imaging filter (Gatan Inc., USA). Details of the measurements are outlined in Additional file 1.

Monte-Carlo simulations

The NISTMonte package [34] was used for MC simulations in this work. NISTMonte contains implemented screened Rutherford cross-sections [35], Mott cross-sections calculated by Czyzewski et al. [36], and cross-sections obtained by semi-empirical fitting by Browning et al. [37] denoted by Browning in the following. The energy loss of electrons is calculated by the Joy-Luo formalism [38]. Table 1 lists materials parameters of PTB7 and $PC_{71}BM$ used for the MC simulations.

For comparison between experimental and simulated STEM intensities, simulated intensities I are normalized with respect to the intensity of the incident electrons (i.e. the total number of simulated electron trajectories) I_0. In addition, the properties of the semiconductor STEM detector must be taken into account. Electrons with energies below the detector cutoff energy E_{cutoff} do not contribute to the measured STEM intensity. These electrons

Table 1 Material parameters of PTB7 and $PC_{71}BM$ used for MC simulations [39]

	Chemical formulae	Density (g/cm³)	Mean atomic number (Z_m)	Mean atomic mass (A_m)
PTB7	$C_{41}H_{53}FS_4O_4$	1.12 ± 0.05	5.30	7.35
$PC_{71}BM$	$C_{82}H_{14}O_2$	1.36 ± 0.05	5.62	10.52

are absorbed by the thin metal protection layer on the detector. The cutoff energy was experimentally determined to be 500 eV. For a semiconductor detector, the energy of the detected electrons also influences the measured STEM intensity. The electron energy determines the number of generated electron–hole pairs which is given by the average energy to generate an electron–hole pair $E_{e/h}$. Hence, the energy of the simulated electrons E_i after propagation through the specimen needs to be taken into account. The normalized STEM intensity obtained by MC simulations can then be calculated according to Eq. (3).

$$\frac{I}{I_0} = \frac{\frac{\sum_i (E_i - E_{cutoff})}{E_{e/h}}}{\frac{N_o(E_0 - E_{cutoff})}{E_{e/h}}} \qquad (3)$$

where N_0 is the total number of simulated electrons with the primary electron energy E_0. The summation in the numerator is performed over the number of electrons i,

Li *et al. Adv Struct Chem Imag*   (2020) 6:2

Page 5 of 12

which are scattered into the scattering angle range covered by the BF- or HAADF-detector segment, respectively. $E_{e/h}$ obviously cancels out and does not need to be explicitly known.

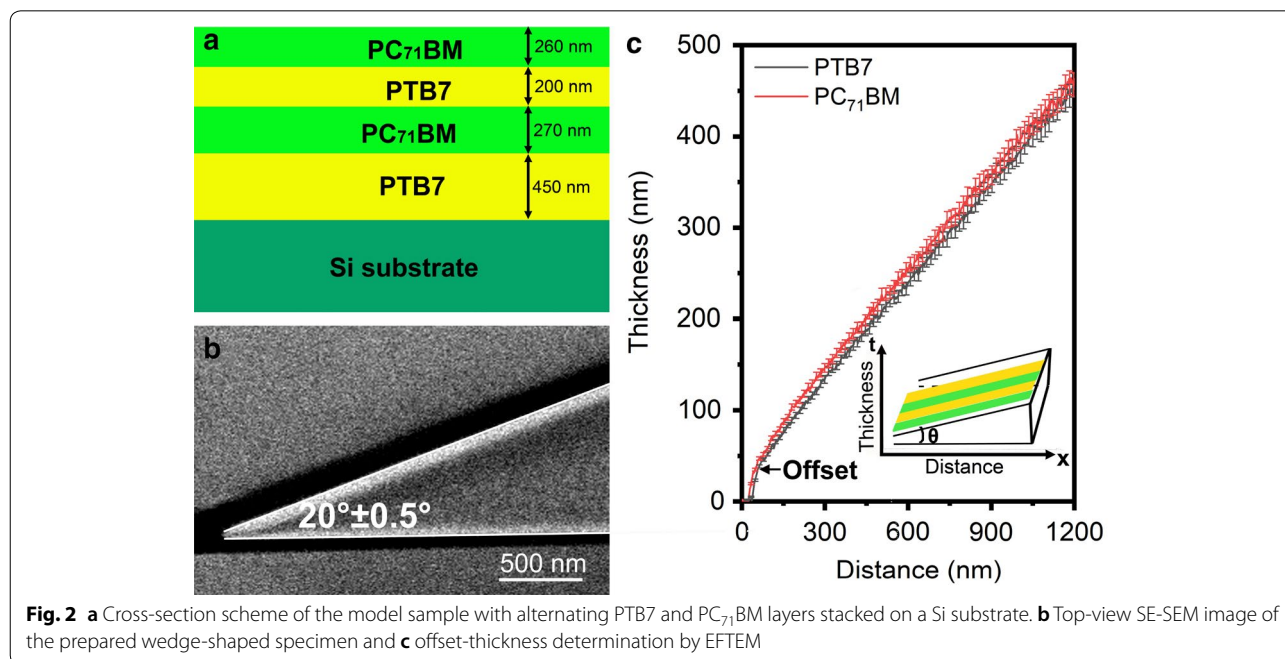## Results and discussion

Methodology considerations

In the following we will present contrast analyses of pure PTB7 and $PC_{71}BM$ with respect to the unambiguous distinction of the two materials and to understand the thickness dependence of BF–STEM and HAADF–STEM intensity. For this purpose, model samples were analyzed which consist of pure PTB7 and $PC_{71}BM$ layers. Figure 2a shows a cross-section scheme of the model specimen with alternating pure PTB7 and $PC_{71}BM$ layers on a Si substrate. Figure 2b presents a top-view SEM image of the prepared wedge-shaped TEM specimen of the model sample with a wedge angle $\theta = 20 \pm 0.5°$. The wedge is not infinitely thin at the edge but is characterized by an offset thickness t_{offset}. Due to the wedge geometry, the local thickness t of the wedge at the distance x from the wedge edge (cf. Fig. 2c) is given by Eq. (4).
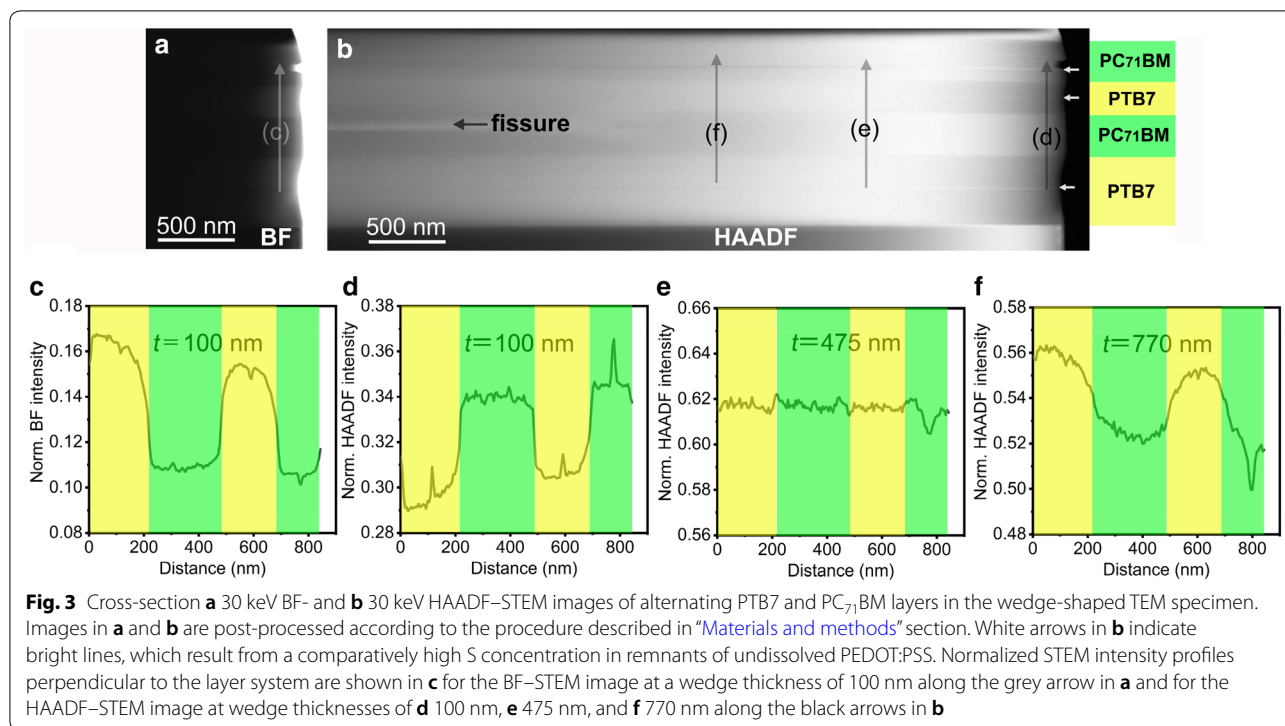
$$t = t_{offset} + x \tan \theta \qquad (4)$$

The offset thickness was determined by EFTEM. A relative thickness map of the wedge sample (cf. Additional file 1: Fig. S1c) was obtained by taking the logarithm of the intensity ratio of the unfiltered (cf. SI Additional file 1: Fig. S1b) and zero-loss filtered image (cf. Additional file 1: Fig. S1a) where each pixel contains

the information on the local sample thickness t in units of the inelastic mean free path λ. For a wedge-shaped sample, the inelastic mean free path λ_{PTB7} and λ_{PC71BM} can be derived from geometric considerations (for details see Additional file 1), and the thickness as a function of the distance x from the wedge edge can be determined (Fig. 2c) with an offset thickness of 40 ± 10 nm. The error of the thickness offset depends on the uncertainty of λ. The error for the thickness indicated by the error bars in Fig. 2c is mainly influenced by the precision of the wedge angle measurement $\pm 0.5°$. The large error for the wedge offset comprises also possible small effects of Ga^+ implantation during the FIB milling.

Figure 3a, b present cross-section 30 keV BF- and HAADF–STEM images of the wedge-shaped model specimen. The arrangement of the PTB7 and $PC_{71}BM$ layers in the wedge is a priori known and illustrated in the scheme at the right side of Fig. 3b. The intensity gradually changes from the wedge edge towards larger thicknesses from right to left to the thickness increase. The layers can be well recognized in the HAADF–STEM image over a large sample thickness range while the BF–STEM intensity (Fig. 3a) rapidly decreases to low values. A region with a fissure in the $PC_{71}BM$ layer is marked by a black arrow (Fig. 3b), which was not considered for intensity measurements. There are also faint bright lines marked by white arrows, which stem from remnants of undissolved PEDOT:PSS with higher average atomic number due to the comparatively

Fig. 2 **a** Cross-section scheme of the model sample with alternating PTB7 and $PC_{71}BM$ layers stacked on a Si substrate. **b** Top-view SE-SEM image of the prepared wedge-shaped specimen and **c** offset-thickness determination by EFTEM

Li *et al. Adv Struct Chem Imag*   (2020) 6:2

Page 6 of 12

Fig. 3 Cross-section **a** 30 keV BF- and **b** 30 keV HAADF–STEM images of alternating PTB7 and PC$_{71}$BM layers in the wedge-shaped TEM specimen. Images in **a** and **b** are post-processed according to the procedure described in "Materials and methods" section. White arrows in **b** indicate bright lines, which result from a comparatively high S concentration in remnants of undissolved PEDOT:PSS. Normalized STEM intensity profiles perpendicular to the layer system are shown in **c** for the BF–STEM image at a wedge thickness of 100 nm along the grey arrow in **a** and for the HAADF–STEM image at wedge thicknesses of **d** 100 nm, **e** 475 nm, and **f** 770 nm along the black arrows in **b**

high S content as confirmed by energy dispersive X-ray (EDXS) mapping in Additional file 1: Fig. S2.

Line profiles of the normalized BF–STEM and HAADF–STEM intensities in Fig. 3c–f are extracted perpendicular to the layer system at different positions (cf. grey arrow in Fig. 3a and black arrows in Fig. 3b). At about 100 nm sample thickness (Fig. 3c), PC$_{71}$BM shows a lower intensity than PTB7 in the BF–STEM image. The layer contrast is inverted in the HAADF–STEM image at the same thickness (Fig. 3d). Sharp peaks in the line profiles originate from thin layers of undissolved PEDOT:PSS. With the thickness increasing to about 475 nm, the BF–STEM intensity becomes too low to distinguish PTB7 and PC$_{71}$BM. The HAADF–STEM intensities of PTB7 and PC$_{71}$BM are higher at a thickness of 475 nm, but the intensities of the two materials are similar and prevent distinction of the layers (Fig. 3e). The contrast between PTB7 and PC$_{71}$BM is inverted at larger thicknesses as illustrated for a sample thickness of 770 nm (Fig. 3f), where PTB7 shows a higher intensity than PC$_{71}$BM. We note that the contrast of the two materials is determined by pure mass–thickness contrast as demonstrated by TED patterns (cf. SI Additional file 1: Fig. S4), which do not show Bragg reflections. This is an indispensable prerequisite for comparing experimental intensities with MC simulations because contributions because the Bragg contrast cannot be simulated.

Figure 4 shows in more detail the behavior of the normalized BF–STEM intensity of PC$_{71}$BM and PTB7 as a function of the sample thickness at 30 keV. The BF–STEM image (inset in Fig. 4) and intensity line profiles
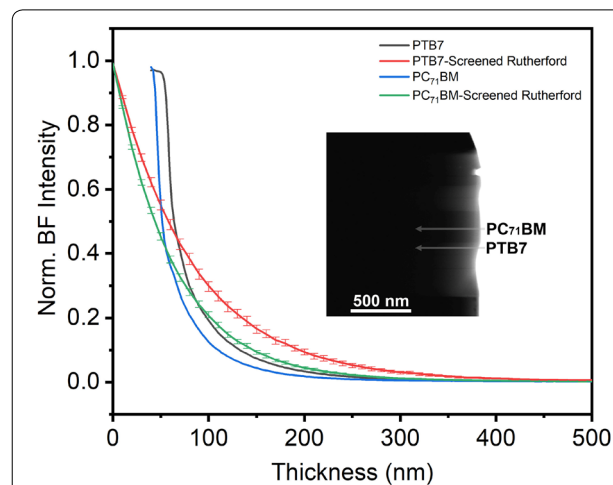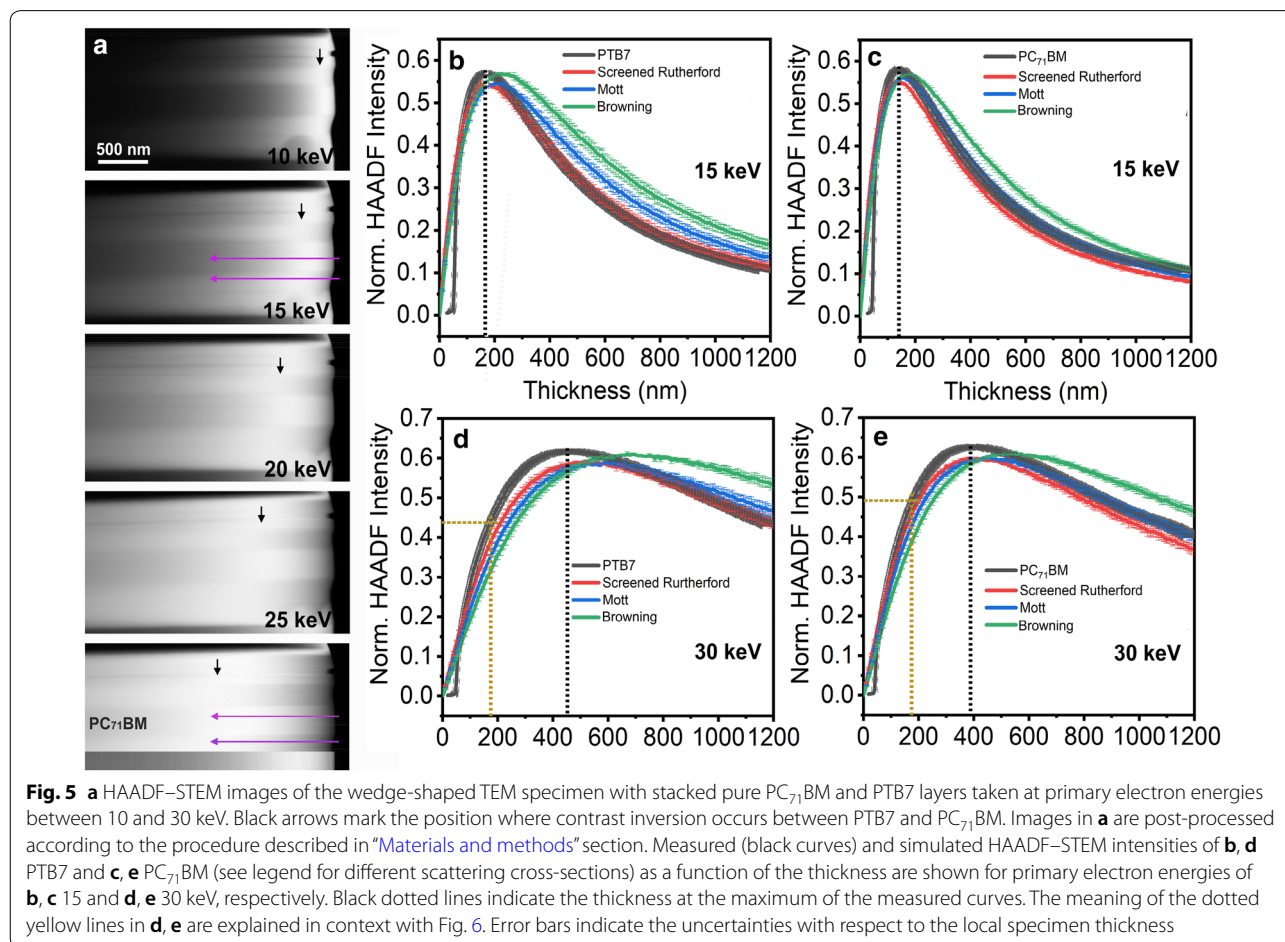

Fig. 4 Line profiles of measured BF–STEM intensity of PTB7 (black line) and PC$_{71}$BM (blue line) and corresponding MC simulations for PTB7 (red line) and PC$_{71}$BM (green line) as a function of the sample thickness for an electron energy of 30 keV. The inset shows the corresponding cross-section BF–STEM image of the wedge-shaped specimen. The arrows mark the positions of the intensity line profiles acquired from the wedge edge along the direction of increasing wedge thickness. Error bars result from the effect of the uncertainty of the material densities given Table 1 on the simulated BF–STEM intensity

show that PTB7 is always brighter than PC$_{71}$BM independent of the specimen thickness without contrast inversion as opposed to the HAADF–STEM intensities. Unambiguous distinction of PTB7 and PC$_{71}$BM is therefore possible based on BF–STEM intensities. However, the intensity drops steeply with increasing sample thickness. The materials become effectively opaque at a thickness exceeding 150 nm due to strong electron scattering in angles beyond the detection-angle range of the BF–STEM detector segment. We note that the maximum scattering angle of the BF–STEM detector is only 6.9 mrad. Using a larger BF–STEM detector would increase sample transparency for BF–STEM imaging. Figure 4 also compares the experimental data with MC simulations using screened Rutherford cross-sections for the MC simulations. Additionally, simulations were performed with Mott and Browning cross-section, which essentially agree with the simulations based on screened Rutherford cross-sections. The simulations reproduce the general behavior of the experimental BF–STEM intensity with PTB7 showing a higher intensity than PC$_{71}$BM. However,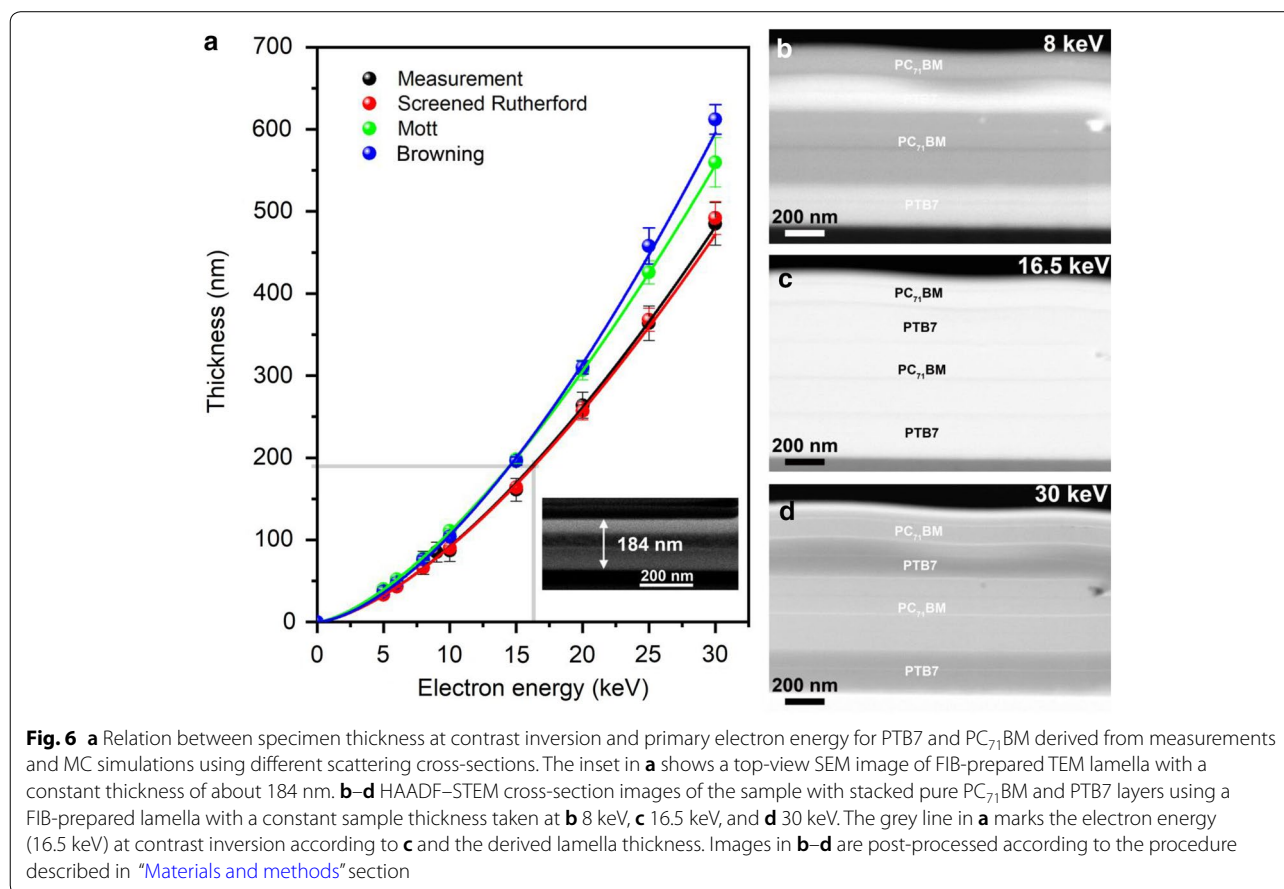 the measured BF–STEM intensities are consistently lower than simulated data, which is mainly attributed to the deviation of the wedge from the perfect shape close to the wedge edge. In fact, the thickness offset of the wedge leads to the steep drop of the experimental BF–STEM intensity (cf. black lines in Fig. 5b–e) at about 50 nm.

Figure 5a presents a series of HAADF–STEM images of the wedge-shaped TEM specimen with stacked pure PC$_{71}$BM and PTB7 layers taken at electron energies between 10 and 30 keV in increments of 5 keV with the thin wedge edge at the right-hand side of the images. At small sample thicknesses, PTB7 appears with lower intensity than PC$_{71}$BM. As already shown in Fig. 3b, a contrast inversion occurs between PTB7 and PC$_{71}$BM at thicknesses that increase with the electron energy (see black arrows in Fig. 5a). Experimental (black curves) and simulated normalized HAADF–STEM intensities of PTB7 and PC$_{71}$BM are shown in Fig. 5b–e as a function of the specimen thickness for 15 and 30 keV, respectively. For clarity, results for PTB7 and PC$_{71}$BM are not presented in the same figure. The HAADF–STEM intensities of PTB7 and PC$_{71}$BM generally show maxima at a

Fig. 5 a HAADF–STEM images of the wedge-shaped TEM specimen with stacked pure PC$_{71}$BM and PTB7 layers taken at primary electron energies between 10 and 30 keV. Black arrows mark the position where contrast inversion occurs between PTB7 and PC$_{71}$BM. Images in **a** are post-processed according to the procedure described in "Materials and methods" section. Measured (black curves) and simulated HAADF–STEM intensities of **b**, **d** PTB7 and **c**, **e** PC$_{71}$BM (see legend for different scattering cross-sections) as a function of the thickness are shown for primary electron energies of **b**, **c** 15 and **d**, **e** 30 keV, respectively. Black dotted lines indicate the thickness at the maximum of the measured curves. The meaning of the dotted yellow lines in **d**, **e** are explained in context with Fig. 6. Error bars indicate the uncertainties with respect to the local specimen thickness

Li *et al. Adv Struct Chem Imag*   (2020) 6:2

Page 8 of 12

thickness that depends on E_0 and the material properties. The intensity first increases with thickness due to enhanced electron scattering into the detection angle range of the HAADF detector segment. The reduction of the HAADF–STEM intensity beyond the maximum is related to the fact that an increasing fraction of electrons is scattered beyond the detection angle range of the HAADF–STEM detector. At 15 keV (Fig. 5b, c), the intensity maxima occur in PTB7 and $PC_{71}BM$ at a sample thickness of 170 and 145 nm. With increasing electron energies, the maxima shift to larger thicknesses of 470 and 400 nm at 30 keV (Fig. 5d, e). The experimental data (black curves in Fig. 5b–e) is reasonably well reproduced by MC simulations based on screened Rutherford cross-sections (red curves in Fig. 5b–e). Slightly larger discrepancies are found for simulations based on Mott cross-sections (blue curves in Fig. 5b–e) while Browning cross-sections (green curves in Fig. 5b–e) generally do not well describe the experimental data. The discrepancies between measured and simulated HAADF–STEM intensities at small thicknesses are mainly attributed to the thickness offset of the wedge and deviations from the ideal wedge shape.

The relation between specimen thickness and electron energy at contrast inversion has to be understood to enable unambiguous material assignment based on HAADF–STEM images and can be also exploited for specimen thickness determination as demonstrated in the following. Figure 6a shows measurements and MC simulations of the thickness at minimum contrast between $PC_{71}BM$ and PTB7 as a function of the electron energy obtained from the wedge-shaped specimen (cf. Fig. 5a). Minimum contrast between PTB7 and $PC_{71}BM$ marks the TEM specimen thickness, where contrast inversion occurs. A power law function of the type $t_{inv} = a \cdot E_0^b$ can be fitted to the experimental and simulated data. Good agreement is obtained between measurements and MC simulations for screened Rutherford cross-sections with $b = 1.50 \pm 0.01$ and $a = 2.91 \pm 0.11$ with electron energies given in keV and thickness at contrast inversion t_{inv} in nm. Discrepancies between experimental data and MC simulations are found for Mott scattering cross-sections ($b = 1.47 \pm 0.01$ and $a = 3.66 \pm 0.09$) and Browning cross-sections ($b = 1.57 \pm 0.02$ and $a = 2.81 \pm 0.14$). The validity of the data in Fig. 6a is

Fig. 6 **a** Relation between specimen thickness at contrast inversion and primary electron energy for PTB7 and $PC_{71}BM$ derived from measurements and MC simulations using different scattering cross-sections. The inset in **a** shows a top-view SEM image of FIB-prepared TEM lamella with a constant thickness of about 184 nm. **b**–**d** HAADF–STEM cross-section images of the sample with stacked pure $PC_{71}BM$ and PTB7 layers using a FIB-prepared lamella with a constant sample thickness taken at **b** 8 keV, **c** 16.5 keV, and **d** 30 keV. The grey line in **a** marks the electron energy (16.5 keV) at contrast inversion according to **c** and the derived lamella thickness. Images in **b**–**d** are post-processed according to the procedure described in "Materials and methods" section

Li *et al. Adv Struct Chem Imag*   (2020) 6:2

Page 9 of 12

tested by the investigation of the PTB7/PC$_{71}$BM layer system using a FIB-prepared TEM lamella with constant thickness. Figure 6b–d present cross-section HAADF–STEM images of this specimen taken at 8, 16.5 and 30 keV. Minimum contrast between PTB7 and PC$_{71}$BM occurs at 16.5 keV (Fig. 6c). The contrast of the two materials is inverted at 8 and 30 keV (Fig. 6b, d). A lamella thickness of 192 nm can be derived (indicated by grey lines Fig. 6a) if minimum contrast occurs at 16.5 keV. This thickness is in good agreement with the thickness determined from a top-view SE-SEM image of the lamella (inset in Fig. 6a). With the TEM lamella thickness marked in Fig. 5d, e by a yellow dotted line, it is clear that PTB7 appears with lower intensity than PC$_{71}$BM at 30 keV (cf. Fig. 6d) while the contrast is inverted at 8 keV (cf. Fig. 6b).

The presented methodology employing low-energy BF- and HAADF-STEM therefore does not only allow to reliably distinguish materials with only slightly different scattering properties, it can be also used to determine the thickness of TEM lamellae with good accuracy.

Application of correlative STEM/SEM to PTB7:PC$_{71}$BM absorber layers

In this section, we demonstrate the application of low-energy STEM to study the effect of different amounts of DIO in the process solvent on nanomorphology formation within PTB7:PC$_{71}$BM bulk-heterojunction absorber layers. Due to the thickness dependence of STEM contrast, correlative SE-SEM images were acquired to obtain information on topography changes, which are useful to interpret the corresponding STEM images.

Figure 7 shows correlative plan-view SE-SEM, BF- and HAADF-STEM images of PTB7:PC$_{71}$BM absorber layers processed from *o*-xylene solution without DIO (Fig. 7a–c), with 1 vol% DIO (Fig. 7d–f) and 3 vol% DIO (Fig. 7g–i). BF–STEM cross-section images of the same absorber layers are presented in Fig. 8a–c to verify the interpretation of the plan-view images. The cross-section images are not affected by specimen thickness changes because they were prepared by FIB milling with a homogeneous thickness. Assuming the same TEM specimen thickness, BF–STEM images allow unambiguous material assignment (cf. Fig. 4) with PC$_{71}$BM exhibiting a lower intensity
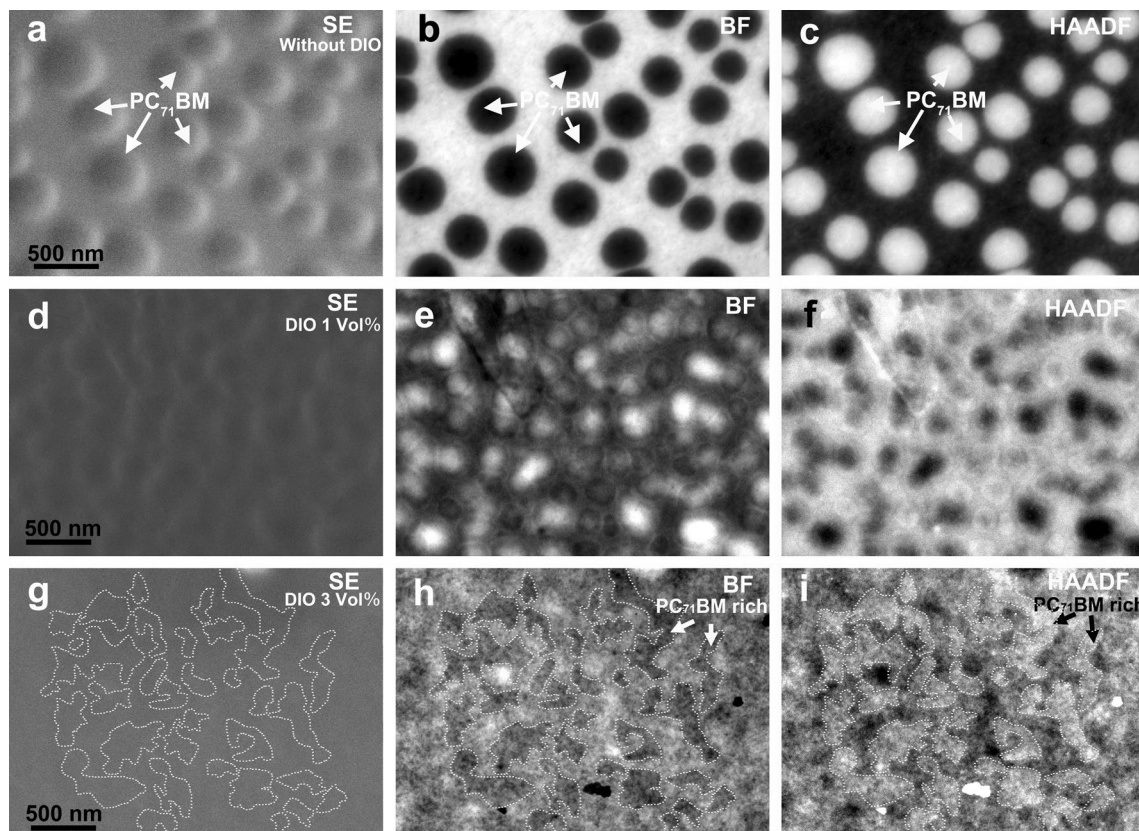

Fig. 7 Plan-view correlative SE-SEM, BF- and HAADF–STEM images of PTB7:PC$_{71}$BM-based absorber layers taken at 30 keV that were processed from *o*-xylene solution **a**–**c** without DIO, **d**–**f** with 1 vol% DIO and **g**–**i** 3 vol% DIO. Images in are post-processed according to the procedure described in "Materials and methods" section
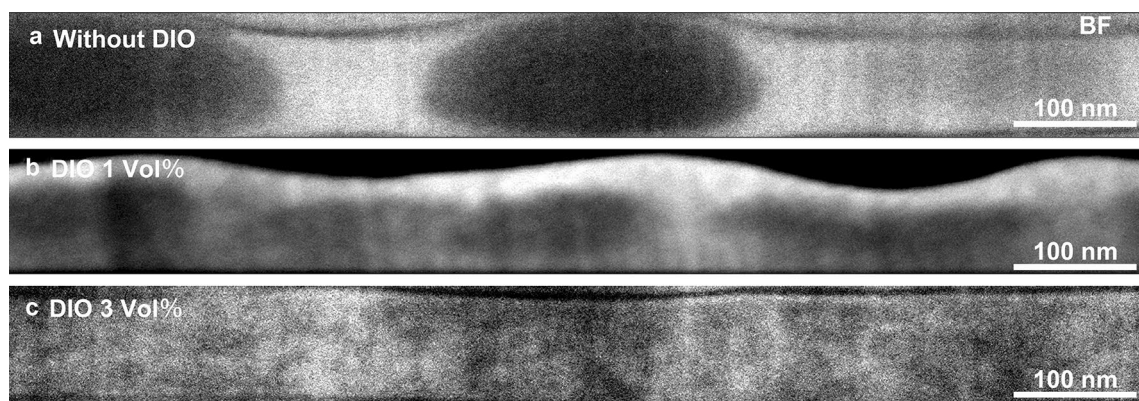
Fig. 8 30 keV cross-section BF–STEM images of PTB7:PC$_{71}$BM absorber layers processed from *o*-xylene solution **a** without DIO, with addition of **b** 1 vol% DIO and **c** 3 vol% DIO. The images were taken from specimens containing several stacked absorber layers. Thin dark layers in (**a**) and (**c**) consist of undissolved remnants of PEDOT:PSS as evidenced by EDXS mapping in Additional file 1: Fig. S3. A Pt protection layer is seen in **b** on the uppermost absorber layer of the stack. Images in **a**–**c** are post-processed according to the procedure described in "Materials and methods" section

than PTB7. The BF–STEM image of the PTB7:PC$_{71}$BM absorber layer without DIO in Fig. 7b suggests that large PC$_{71}$BM domains (200–500 nm) are embedded in the PTB7 matrix. The contrast is inverted in the HAADF–STEM image in Fig. 7c as expected. The corresponding SE-SEM image Fig. 7a suggests an elevated island-like topography of the PC$_{71}$BM domains, which even further reduces the BF–STEM intensity of PC$_{71}$BM according to Fig. 4. This interpretation is supported by the cross-section image Fig. 8a showing lens-shaped PC$_{71}$BM domains embedded in PTB7 consistent with previous work by Liang et al. [32].

A pronounced topography is also recognizable in the SE-SEM image of the absorber layer that was processed from *o*-xylene solution with 1 vol% DIO (cf. Fig. 7d). The BF–STEM image Fig. 7e seems to indicate that bright regions consisting of PTB7 are embedded in PC$_{71}$BM. However, SE-SEM shows that bright regions are correlated with depressions in the surface topography, which could induce a contrast reversal between PC$_{71}$BM and PTB7. The cross-section BF–STEM image in Fig. 8b indeed shows pronounced thickness variations of the absorber layer and PC$_{71}$BM domains with dark contrast and sizes of 200–500 nm that are frequently located in thinner regions of the absorber layer. This indeed leads to contrast reversal in the BF–STEM image (cf. Fig. 7e) where PC$_{71}$BM appears with higher intensity compared to PTB7. Contrast reversal, as expected, occurs in the HAADF–STEM image Fig. 7f.

The addition of 3 vol% DIO leads to a drastic nanomorphology change with an almost homogeneous absorber layer thickness (SE-SEM image in Fig. 7g and BF–STEM image in Fig. 8c). PC$_{71}$BM-rich regions with lower intensity are marked in the BF–STEM image Fig. 7h by dotted lines. These regions show intensity variations, which can be attributed to a domain substructure with typical domains sizes in the few 10 nm range, which are also recognizable in the cross-section BF–STEM image Fig. 8c.

Sprau et al. [33] have investigated the power conversion efficiency (PCE) of organic solar cells containing absorber layers with the same properties as those investigated in this work. Solar cells with absorber layers processed from *o*-xylene solution without DIO showed a PCE of only 2.2%, which is attributed to the formation of large fullerene domains within the bulk-heterojunction. The PCE increased to 4.1% upon addition of 1 vol% DIO to the *o*-xylene solution. The substantial PCE increase cannot be attributed to the reduction of the domain sizes, which are similar as in the photoactive layer without DIO but it could be related to a certain PC$_{71}$BM content in the PTB7 matrix. A high PCE of 7.0% was measured for solar cells with the photoactive layer containing 3 vol% DIO. The PCE improvement in this layer was attributed to a small-scale domain structure in horizontal and vertical direction as confirmed in this work. Exciton diffusion lengths are between 5 and 15 nm [40], which are of the same order of magnitude as the domain sizes of a few 10 nm. This morphology supports efficient transport of photo-generated charge carriers to the electrodes, which is essential for the optimization of photovoltaic performance.

Summary and conclusions

The benefits of correlative low-energy STEM/SEM are demonstrated on PTB7:PC$_{71}$BM bulk-heterojunction absorber layers, which are commonly employed in organic solar cells. The main results can be summarized as follows:

Li *et al. Adv Struct Chem Imag* (2020) 6:2

Page 11 of 12

- Sensitive material BF- and HAADF-STEM contrast allows to clearly distinguish weakly scattering materials like $PC_{71}BM$ and PTB7 with similar material properties.
- When comparing PTB7 and $PC_{71}BM$, BF–STEM allows unambiguous material identification because PTB7 always shows a higher intensity than $PC_{71}BM$ independent of the specimen thickness. Contrast inversion between PTB7 and $PC_{71}BM$ occurs in HAADF–STEM images at a TEM specimen thickness that depends on the electron energy. The relation between electron energy and thickness at contrast inversion can be exploited for specimen thickness determination.
- MC simulations are required for contrast interpretation of low-energy STEM images. The results of MC simulations depend on the type of scattering cross-section with screened Rutherford scattering cross-section yielding the best agreement with experimental data for the studied materials.
- Correlative STEM/SEM applied to $PTB7:PC_{71}BM$ absorber layers yields bulk and topography information from the same specimen region, which is helpful to recognize contrast changes induced by thickness variations of the TEM sample.
- Different DIO contents in the *o*-xylene solution, from which the $PTB7:PC_{71}BM$ absorber layers were deposited, strongly influence the nanomorphology (surface topography and domain sizes). Large-scale phase separation with island-like $PC_{71}BM$ inclusions in PTB7 is observed in blends that were processed without DIO. The nanomorphology changes drastically with 3 vol% DIO addition where a flat surface topography and domains with sizes of only a few 10 nm correlate with a strong PCE increase.

Overall, our results suggest that low-energy correlative SEM/STEM is well-suited to image beam-sensitive, weakly scattering and complex organic materials. Combination with FIB-based TEM sample preparation is advantageous for materials that should not be exposed to air because they can be investigated in the same instrument. The resolution is still inferior compared to high-energy STEM but it could be improved by an aberration corrector implemented in the SEM column.

Supplementary information

Supplementary information accompanies this paper at https://doi.org/10.1186/s40679-020-00069-4.

> **Additional file 1:** Thickness determination of the wedge specimen by EFTEM and phase identification of the absorber layer by STEM-EDXS mapping.

Abbreviations
BF: Bright field; HAADF: High angle annular dark field; SE-SEM: Secondary electron scanning electron microscopy; STEM: Scanning transmission electron microscopy; DIO: 1,8-Diiodooctance; BHJ: Bulk-heterojunction; MC: Monte-Carlo; ITO: Indium tin oxide; CCD camera: Charge-coupled device camera; FIB: Focused-ion beam; TED: Transmission electron diffraction; TEM: Transmission electron microscopy; ETD: Everhart–Thornley detector; EFTEM: Energy-filtered transmission electron microscopy; EDXS: Energy dispersive X-ray spectroscopy.

Authors' contributions
DG, EM, YL conceived the project and experiment. YL prepared the FIB samples and performed the (S) TEM experiments and simulations. EM provided useful suggestions on Monte-Carlo simulations. CS and AC provided the absorber layer samples for characterization. The manuscript was written by YHL and DG. All authors read and approved the final manuscript.

Availability of data and materials
All the reach data in this study can be provided by the corresponding author upon reasonable requests.

Competing interests
The authors declare that they have no competing interests.

Author details
[1] Laboratory for Electron Microscopy, Karlsruhe Institute of Technology (KIT), Engesserstr. 7, 76131 Karlsruhe, Germany. [2] Light Technology Institute, Karlsruhe Institute of Technology (KIT), Engesserstr. 13, 76131 Karlsruhe, Germany. [3] Material Research Center for Energy Systems (MZE), Karlsruhe Institute of Technology (KIT), Strasse am Forum 7, 76131 Karlsruhe, Germany. [4] DFG Cluster of Excellence 3D Matter Made to Order, Karlsruhe Institute of Technology (KIT), Karlsruhe, Germany.

References
1. Kaiser, U., Biskupek, J., Meyer, J., Leschner, J., Lechner, L., Rose, H., Stöger-Pollach, M., Khlobystov, A., Hartel, P., Müller, H.: Transmission electron microscopy at 20 kV for imaging and spectroscopy. Ultramicroscopy **111**, 1239–1246 (2011)
2. Bell, D.C., Mankin, M., Day, R.W., Erdman, N.: Successful application of Low Voltage Electron Microscopy to practical materials problems. Ultramicroscopy **145**, 56–65 (2014)
3. Bell, D.C., Erdman, N.: Low voltage electron microscopy: principles and applications. John Wiley, Chichester (2012)
4. Sun, C., Müller, E., Meffert, M., Gerthsen, D.: On the progress of scanning transmission electron microscopy (STEM) imaging in a scanning electron microscope. Microsc. Microanal. **24**, 99–106 (2018)
5. Konno, M., Ogashiwa, T., Sunaoshi, T., Orai, Y., Sato, M.: Lattice imaging at an accelerating voltage of 30 kV using an in-lens type cold field-emission scanning electron microscope. Ultramicroscopy **145**, 28–35 (2014)
6. Zhu, Y., Inada, H., Nakamura, K., Wall, J.: Imaging single atoms using secondary electrons with an aberration-corrected electron microscope. Nat. Mater. **8**, 808 (2009)
7. Inada, H., Su, D., Egerton, R., Konno, M., Wu, L., Ciston, J., Wall, J., Zhu, Y.: Atomic imaging using secondary electrons in a scanning transmission electron microscope: experimental observations and possible mechanisms. Ultramicroscopy **111**, 865–876 (2011)

8. Krumeich, F., Müller, E., Wepf, R.A., Nesper, R.: Characterization of catalysts in an aberration-corrected scanning transmission electron microscope. J. Phys. Chem. C **115**, 1080–1083 (2010)
9. Golla, U., Schindler, B., Reimer, L.: Contrast in the transmission mode of a low-voltage scanning electron microscope. J. Microsc. **173**, 219–225 (1994)
10. Merli, P., Migliori, A., Nacucchi, M., Antisari, M.V.: Comparison of spatial resolutions obtained with different signal components in scanning electron microscopy. Ultramicroscopy **65**, 23–30 (1996)
11. Klein, T., Buhr, E., Frase, C.G.: TSEM: A review of scanning electron microscopy in transmission mode and its applications. Advances in imaging and electron physics, pp. 297–356. Elsevier, Berlin (2012)
12. Buhr, E., Senftleben, N., Klein, T., Bergmann, D., Gnieser, D., Frase, C., Bosse, H.: Characterization of nanoparticles by scanning electron microscopy in transmission mode. Meas. Sci. Technol. **20**, 084025 (2009)
13. Klein, T., Buhr, E., Johnsen, K., Frase, C.: Traceable measurement of nanoparticle size using a scanning electron microscope in transmission mode (TSEM). Meas. Sci. Technol. **22**, 094002 (2011)
14. Sun, C., Müller, E., Meffert, M., Gerthsen, D.: Analysis of crystal defects by scanning transmission electron microscopy (STEM) in a modern scanning electron microscope. Adv. Struct. Chem. Imag. **5**, 1 (2019)
15. Schweizer, P., Dolle, C., Spiecker, E.: In situ manipulation and switching of dislocations in bilayer graphene. Sci. Adv. **4**, eaat4712 (2018)
16. Callahan, P.G., Stinville, J.-C., Yao, E.R., Echlin, M.P., Titus, M.S., De Graef, M., Gianola, D.S., Pollock, T.M.: Transmission scanning electron microscopy: defect observations and image simulations. Ultramicroscopy **186**, 49–61 (2018)
17. Stinville, J., Yao, E.R., Callahan, P.G., Shin, J., Wang, F., Echlin, M.P., Pollock, T.M., Gianola, D.S.: Dislocation dynamics in a nickel-based superalloy via in situ transmission scanning electron microscopy. Acta Mater. **168**, 152–166 (2019)
18. Volkenandt, T., Müller, E., Hu, D., Schaadt, D., Gerthsen, D.: Quantification of sample thickness and In-concentration of InGaAs quantum wells by transmission measurements in a scanning electron microscope. Microsc. Microanal. **16**, 604–613 (2010)
19. Drees, H., Müller, E., Dries, M., Gerthsen, D.: Electron-beam broadening in amorphous carbon films in low-energy scanning transmission electron microscopy. Ultramicroscopy **185**, 65–71 (2018)
20. Hugenschmidt, M., Müller, E., Gerthsen, D.: Electron beam broadening in electron-transparent samples at low electron energies. J. Microsc. **274**, 150–157 (2019)
21. Volkenandt, T., Müller, E., Gerthsen, D.: Sample thickness determination by scanning transmission electron microscopy at low electron energies. Microsc. Microanal. **20**, 111–123 (2014)
22. Brodusch, N., Demers, H., Gelle, A., Moores, A., Gauvin, R.: Electron energy-loss spectroscopy (EELS) with a cold-field emission scanning electron microscope at low accelerating voltage in transmission mode. Ultramicroscopy **203**, 21–36 (2019)
23. Pfaff, M., Klein, M.F., Müller, E., Müller, P., Colsmann, A., Lemmer, U., Gerthsen, D.: Nanomorphology of P3HT: PCBM-based absorber layers of organic solar cells after different processing conditions analyzed by low-energy scanning transmission electron microscopy. Microsc. Microanal. **18**, 1380–1388 (2012)
24. Heeger, A.J.: 25th anniversary article: bulk heterojunction solar cells: understanding the mechanism of operation. Adv. Mater. **26**, 10–28 (2014)
25. Treat, N.D., Varotto, A., Takacs, C.J., Batara, N., Al-Hashimi, M., Heeney, M.J., Heeger, A.J., Wudl, F., Hawker, C.J., Chabinyc, M.L.: Polymer-fullerene miscibility: a metric for screening new materials for high-performance organic solar cells. J. Am. Chem. Soc. **134**, 15869–15879 (2012)
26. van-Bavel, S.S., Sourty, E., Loos, J.: Three-dimensional nanoscale organization of bulk heterojunction polymer solar cells. Nano Lett. **9**, 507–513 (2009)
27. Leijten, Z.J., Keizer, A.D., de With, G., Friedrich, H.: Quantitative analysis of electron beam damage in organic thin films. J. Phys. Chem. C **121**, 10552–10561 (2017)
28. Libera, M.R., Egerton, R.F.: Advances in the transmission electron microscopy of polymers. Polym. Rev. **50**, 321–339 (2010)
29. Moon, J.S., Takacs, C.J., Sun, Y., Heeger, A.J.: Spontaneous formation of bulk heterojunction nanostructures: multiple routes to equivalent morphologies. Nano Lett. **11**, 1036–1039 (2011)
30. Liu, F., Zhao, W., Tumbleston, J.R., Wang, C., Gu, Y., Wang, D., Briseno, A.L., Ade, H., Russell, T.P.: Understanding the morphology of PTB7: PCBM blends in organic solar cells. Adv. Energy Mater. **4**, 1301377 (2014)
31. Klein, M.F., Pfaff, M., Müller, E., Czolk, J., Reinhard, M., Valouch, S., Lemmer, U., Colsmann, A., Gerthsen, D.: Poly (3-hexylselenophene) solar cells: correlating the optoelectronic device performance and nanomorphology imaged by low-energy scanning transmission electron microscopy. J. Polym. Sci. B Polym. Phys. **50**, 198–206 (2012)
32. Liang, Y., Xu, Z., Xia, J., Tsai, S.T., Wu, Y., Li, G., Ray, C., Yu, L.: For the bright future—bulk heterojunction polymer solar cells with power conversion efficiency of 7.4%. Adv. Mater. **22**, E135–E138 (2010)
33. Sprau, C., Buss, F., Wagner, M., Landerer, D., Koppitz, M., Schulz, A., Bahro, D., Schabel, W., Scharfer, P., Colsmann, A.: Highly efficient polymer solar cells cast from non-halogenated xylene/anisaldehyde solution. Energy Environ. Sci. **8**, 2744–2752 (2015)
34. Ritchie, N.W.: A new Monte Carlo application for complex sample geometries. Surf. Interface Anal. **37**, 1006–1011 (2005)
35. Heinrich, K.F.: Electron beam X-ray microanalysis. Van Nostrand Reinhold Company, NewYork (1981)
36. Czyżewski, Z., MacCallum, D.O.N., Romig, A., Joy, D.C.: Calculations of Mott scattering cross section. J. Appl. Phys. **68**, 3066–3072 (1990)
37. Browning, R., Li, T., Chui, B., Ye, J., Pease, R., Czyżewski, Z., Joy, D.: Empirical forms for the electron/atom elastic scattering cross sections from 0.1 to 30 keV. J. Appl. Phys. **76**, 2016–2022 (1994)
38. Joy, D., Luo, S.: An empirical stopping power relationship for low-energy electrons. Scanning **11**, 176–180 (1989)
39. Mateker, W.R., Heumueller, T., Cheacharoen, R., Sachs-Quintana, I., McGehee, M.D., Warnan, J., Beaujuge, P.M., Liu, X., Bazan, G.C.: Molecular packing and arrangement govern the photo-oxidative stability of organic photovoltaic materials. Chem. Mater. **27**, 6345–6353 (2015)
40. Menke, S.M., Holmes, R.J.: Exciton diffusion in organic photovoltaic cells. Energy Environ. Sci. **7**, 499–512 (2014)

Publisher's Note